Materials Science & Engineering A 821 (2021) 141567

Contents lists available at ScienceDirect

Materials Science & Engineering A

journal homepage: www.elsevier.com/locate/msea

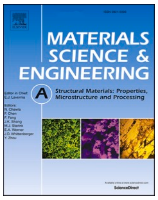

Study on the effects of manganese on the grain structure and mechanical properties of Mg-0.5Ce alloy

Shibo Zhou [a], Peng Peng [b], Jianyue Zhang [c], Tingting Liu [d,*], Guangmin Sheng [a], Jia She [a,e], Fusheng Pan [a,e]

[a] College of Materials Science and Engineering, Chongqing University, Chongqing, 400044, China
[b] School of Metallurgy and Materials Engineering, Chongqing University of Science and Technology, Chongqing 401331, China
[c] Department of Materials Science and Engineering, The Ohio State University, Columbus, OH, 43210, USA
[d] School of Materials and Energy, Southwest University, Chongqing, 400715, China
[e] National Engineering Research Center for Magnesium Alloys, Chongqing University, Chongqing, 400044, China

ARTICLE INFO

Keywords:
Mg alloy
Extrusion
Microstructure
Mechanical properties
Sandwich-like grain structure

ABSTRACT

A novel sandwich grain structure of an Mg–Mn–Ce alloy was achieved by controlling the content of Mn in the traditional extrusion process. The solid-state Mn was dynamically precipitated during the extrusion. These finely precipitated particles hindered the grain boundary migration and refined the dynamically recrystallized grains. A sandwich-like grain structure was formed in as-extruded Mg–Mn–Ce alloys with Mn content increasing from 0.3 wt% to 0.9 wt%. This sandwich-like grain structure induced a tensile yield stress (TYS) that was improved from 86.5 MPa to 166.7 MPa; the Mg-0.9Mn-0.5Ce alloy exhibited improved yield isotropy. Here we discuss the formation mechanism for the sandwich-like grain structure and the strengthening mechanism in detail.

1. Introduction

Magnesium (Mg) alloys, owing to their low density, high specific strength, high thermal conductivity, and satisfactory damping capacity, are widely used in the automotive, aerospace, and mobile electronics industries [1–3]. However, large-scale application of Mg alloys is limited by their poor room-temperature formability. Although wrought Mg alloys have better mechanical properties compared with cast alloys, the Mg alloy sheets usually possess limited ductility during the hot deformation process. This is mainly attributed to the limited availability of slip systems (mostly basal slip) for hexagonal close-packed (hcp) structures [4–6]. Thus, extensive studies have been undertaken to enhance the mechanical properties of wrought Mg alloys [7–9].

The addition of solid solution elements [10–14] is a promising method to improve the formability of Mg alloys at room temperature. Rare earth (RE) elements are commonly used in Mg alloys to improve their ductility, because RE elements can increase the activity of non-basal slip systems [14–17]. For instance, Wu et al. [17] found easy cross-slip of <c+a> dislocations in Mg–Y binary alloys and an improved ductility compared to pure Mg. Huang et al. [18] also pointed out that the prismatic and pyramidal <c+a> slips are more active with the addition of Y. With the addition of Gd [19,20], Er [21], and Ce [22,23], similar activation of non-basal slip systems is also reported in recent research. Therefore, adding RE elements can potentially become a method for producing high-ductility Mg alloys, though their application is limited by the cost of RE elements.

It is reported [24] that some non-RE elements can also be effective at enhancing ductility in the solid state; this is the case for Sn, Zn, Al, Ca, and Mn. Among these elements, Mn is considered to be promising according to recent studies [25–29]. Mn has low solubility in Mg alloys (about ~2.22 wt% at 650 °C). It was originally added to form an intermediate compound with Fe and Si for the purification of Mg [30–32]. Later, it was found that Mn addition can also enhance the strength and ductility of Mg alloys. Yu et al. [33] pointed out that a high density of fine Mn precipitates during extrusion could refine the grains of Mg alloys and improve their mechanical performance. Most recently, the change in critical shear stress (CRSS) of basal slip resistance for alloy elements with maximum solid solubility has been calculated using first principles [34–36]. This work shows that Al, Zn, Y, Gd, Mn, Yb, Ag, Dy, and Er can increase the sliding resistance of basal slip and decrease the difference between the CRSS of basal slip and non-basal slip, which can activate more slip systems and improve their ductility and strength. Among these

---

* Corresponding author.
E-mail addresses: ttliu@swu.edu.cn (T. Liu), fspan@cqu.edu.cn (F. Pan).

https://doi.org/10.1016/j.msea.2021.141567
Received 2 March 2021; Received in revised form 1 June 2021; Accepted 5 June 2021
Available online 14 June 2021

elements, Mn is the lowest-cost element, which means that it is possible to create a high-ductility, low-cost Mg alloy. In addition, the extruded texture can be modified with the addition of Mn. Zhao et al. [28] reported that the as-extruded alloy with 0.5 wt% of added Mn has an elongation of more than 50% due to the favored orientation for basal slip and the reduction of twinning. Hu et al. [27] also found that Mg-0.4Al-1.5Mn alloy shows an excellent failure elongation of 52.5% owing to fine grain size and the high Schmid factor (SF) of non-basal slips. The above studies focus on the improvement of mechanical properties. However, the role of Mn in solid solution in the microstructural evolution during extrusion, as well as the effect on the improvement of mechanical properties, has not been well studied.

In this paper, the influences of different Mn concentrations in solid solution (0.3, 0.6, 0.9 wt%) on a Mg-(0.5 wt%) Ce alloy are studied. The Mn is dissolved into the matrix with a solid solution treatment and then extruded into sheets with the conventional extrusion method. The evolution of the alloy microstructure with as a function of Mn content, as well as the related mechanical properties, is discussed in detail.

2. Experimental

Commercially pure Mg (99.97 wt%), Mg-(3 wt%) Mn, and Mg-(30 wt %) Ce master alloys were used to make the Mg-xMn-(0.5 wt%) Ce alloys (where x = 0.3, 0.6, and 0.9 wt%). These master alloys were melted at 720 °C in a crucible in an electrical furnace with a protective atmosphere of CO_2 and SF_6. Then the crucible was cooled in hot salt water to obtain the ingot. The compositions of these ingots were determined by X-ray fluorescence spectrometry (XRF), and these data are presented in Table 1. Next, these ingots were treated in solid solution at 530 °C for 12h and quenched in cold water. After preheating at 400 °C for 2h, the ingots were extruded at 400 °C using an XJ-500 horizontal extruder with 3 m/min ram speeds and 30 extrusion ratios. The size of the sheets was 56 mm in width and 3 mm in thickness.

Tensile samples with a gauge length of 14 mm and a width of 6 mm were machined from the as-extruded sheet, with direction tilting of 0°, 45°, and 90° to the original extrusion direction (ED). A CMT6305-300 KN testing machine was used to conduct tensile tests with a speed of 1.5 mm/min at room temperature. In the mechanical property tests, three samples were tested and the average value was then obtained. The second phase was analyzed by an X-ray diffractometer (XRD, D/Max 2500 PC). The microstructures of the as-cast, as-solid solution, and as-extruded alloys were determined by scanning electron microscopy (SEM, JEOL JSM-7800F) combined with energy-dispersive X-ray spectroscopy. The optical microscopy (OM) was used to observe microstructures (OLYMPUS OSL4000). For SEM and OM observations, the samples were first ground and then etched in alcohol solution containing 4% of nitric acid.. Image Pro Plus software was used to measure the average grain size of the alloys in representative OM images (for at least five images). For electron backscatter diffraction analysis, the samples were prepared by metallurgical polishing and electro-polishing in an AC2 electrolyte. Electron backscattered diffraction (EBSD) data were obtained from the SEM, and then analyzed with HKL-Channel 5 software. The observed microstructure direction was parallel to the extrusion direction (ED-ND) for all samples.

The anisotropy test was carried out on the tensile sample. True strains following the sheet width (ε_w) and thickness (ε_t) were performed on the samples deformed at a tensile strain of 8%. Lankford *r*-values were obtained using equations (1) and (2) [37]:

$$r = \frac{\varepsilon_w}{\varepsilon_t} = \frac{\ln b/b_0}{\ln t/t_0} \tag{1}$$

$$\Delta r = \frac{1}{2}\left| r_0 - r_{90} - r_{45} \right| \tag{2}$$

Table 1
Chemical compositions of the as-cast Mg–Mn–Ce alloys (wt.%).

Alloys	Chemical composition		
	Mn (wt.%)	Ce (wt.%)	Mg (wt.%)
Mg-0.3Mn-0.5Ce	0.30	0.46	Bal.
Mg-0.6Mn-0.5Ce	0.60	0.45	Bal.
Mg-0.9Mn-0.5Ce	0.86	0.48	Bal.

3. Results

3.1. Phase composition of Mg–Mn–Ce alloys

Fig. 1 exhibits the phase diagram of Mg-xMn-0.5Ce alloys and the XRD patterns of the as-solid solution Mg-xMn-0.5Ce alloys. In Fig. 1a, the thermodynamics equilibrium calculation results show that the second phase in Mg-rich side are Mg12Ce and α-Mn. Meanwhile, the Mn of the designed alloys can be totally dissolved in the Mg matrix at 530 °C as marked by the red lines. From the XRD patterns, the position of diffraction for all solid-solution alloys is similar. The $Mg_{12}Ce$ phases are detected in the three alloys, while α-Mn is not found. This indicates that α-Mn is completely solid in the Mg matrix, which is consisted with the calculation results in Fig. 1a.

3.2. Microstructures

Fig. 2 shows OM images of the as-cast Mg-xMn-(0.5 wt%) Ce alloys (x = 0.3, 0.6, 0.9 wt%). The Mg-0.3Mn-0.5Ce alloy shows a structure similar to a columnar crystal (Fig. 2a). With the increase in Mn content, the grain morphology of the alloys can be changed from a columnar crystal to a dendrite (Fig. 2c and e). According to the SEM-BSE results (Fig. 2b, d, and f), the second-phase particles are uniformly distributed in the Mg matrix. The EDS results in Fig. 2b indicate that they are mainly composed of $Mg_{12}Ce$ and α-Mn, as shown by points A and B in Fig. 2b.

To observe the α-Mn dissolved in α-Mg, the SEM and EDS mapping of solid-solution Mg-xMn-0.5Ce alloys is shown in Fig. S1. After homogenization, the fraction of the second-phase particles is not significantly changed, as shown in Figs. S1a–c. Some second phases remain randomly distributed. The particles have block-shaped morphologies and a size of over 1 μm. According to EDS mapping results (Figs. S1d–f), these block-shaped particles are concentrated with Ce, so we conclude that the block-shaped particles are $Mg_{12}Ce$. This also illustrates that the Mn atoms are completely dissolved in the three alloys, which is consistent with the phase diagram and the XRD results.

A large-scale OM image of the as-extruded alloy was taken on the ND-ED planes, as illustrated in Fig. 3. The observed area spans the distance from the surface to the center of the sheets. It can be seen that a fine and equiaxial grain structure is formed in the Mg-0.3Mn-0.5Ce and Mg-0.6Mn-0.5Ce alloys. The average grain sizes are refined from 12.08 μm in Mg-0.3Mn-0.5Ce to 6.38 μm in Mg-0.6Mn-0.5Ce. However, in the Mg-0.9Mn-0.5Ce alloy, a bimodal grain structure can be seen, which is consistent with elongated, un-dynamic, recrystallized (un-DRXed) grains and some fine grains. These fine grains are around the un-DRXed grain and also exist on the surface of the sheet. The average size of the fine grains is 3.85 μm. This kind of structure is similar to a sandwich structure, which consists of a fine grain in the surface layer and a center part with a bimodal grain structure. The thickness of the surface layer is about ~350 μm. The formation mechanism for this special structure will be explained in section 4.1.

In order to observe the distribution of the second phase after extrusion, the SEM results of as-extruded Mg-xMn-0.5Ce alloys are exhibited in Fig. S2. It is clear that the coarse second-phase particles are broken apart during the extrusion. From Fig. S2a, which shows the Mg-0.3Mn-0.5Ce alloy, it is clear that these broken fine particles are discontinuously distributed along the extrusion direction. This phenomenon also exists in the Mg-0.6Mn-0.5Ce alloy in Fig. S2b. In the Mg-0.9Mn-0.5Ce alloy, the surface area also contains discontinuously distributed fine

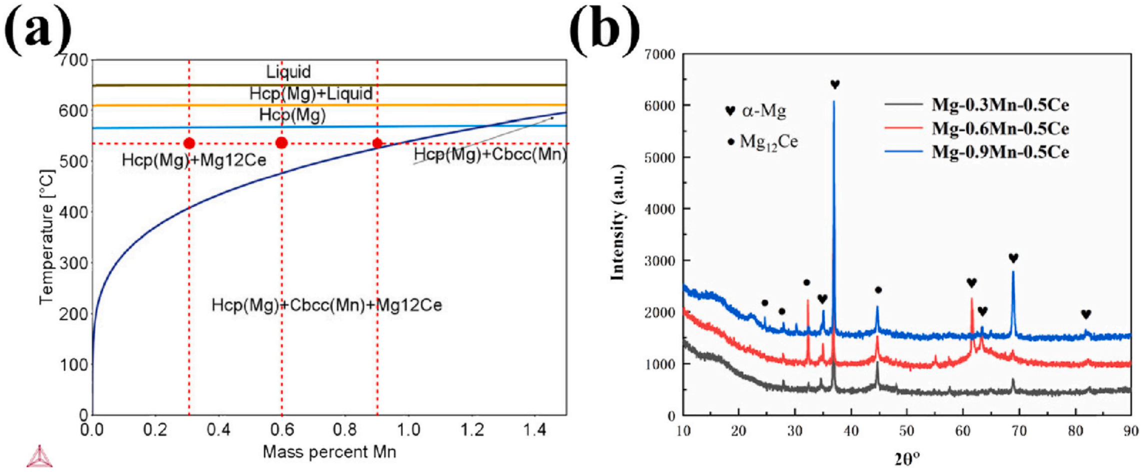

Fig. 1. (a) Phase diagram of Mg-xSc alloys, (b) XRD patterns of the solid-solution Mg-xMn-0.5Ce alloys (x = 0.3, 0.6, 0.9 wt%).

particles (Fig. S2c), while the particles at the center part are continuously distributed (Fig. S2d). This shows that the surface of the Mg-0.9Mn-0.5Ce sheet may be subjected to higher stress, which results in more fragmented second-phase particles. The center part may be subjected to lower stress, which cannot break the bigger, second-phase particles. This also implies that the strain is uniformly distributed from the surface to the center.

Fig. 4 shows bright-field TEM (BF-TEM) images of the as-extruded Mg-0.9Mn-0.5Ce alloy. Fig. 4a shows that both micron-scale (as marked by the red line) and nanoscale particles are found in the matrix. Meanwhile, some nanoscale particles are inside of the micron-scale particles. From the EDS results in Fig. 4b and c, the nanoscale particles in the matrix are identified as $Mg_{12}Ce$ phase and α-Mn. The micron-scale particles are identified as a $Mg_{12}Ce$ phase, according to the EDS results from point 2 in Fig. 4c. Also, the results from points 2 and 3 indicate that α-Mn and Mg are oriented in a certain way with respect to one another. These orientation relationships (OR) for Mg and α-Mn precipitates were previously observed in Fig. 4c. For OR (parallel to the c-axis [0001] of Mg) they are: $\{201\}_{Mn}||\{01\text{–}10\}_{Mg}$, $\{021\}_{Mn}||\{\text{-}1103\}_{Mg}$. Fig. S3 shows High Angle Annular Dark Field Imaging (HADDF) and EDS mapping images of the Mg-0.9Mn-0.5Ce alloy. Besides the micro-scale $Mg_{12}Ce$ particles, many nano-scale α-Mn precipitates are also observed.

It was found that some of the nanoparticles were sheared by dislocation during the extrusion process (see Fig. S4). Recent studies [38–41] have shown that under certain conditions, precipitates in Mg alloys may be shearable. The conditions that determine whether a precipitate can be sheared are the shape of the precipitates, the size of the precipitates, and the degree of crystal mismatch between the precipitates and the matrix. Fig. S4a shows the second-phase pinning of the dislocation, which can hinder the movement of dislocations. Hence, dislocations are becoming tangled with each other. The high-resolution TEM images of Figs. S4b and S4c show that dislocations shear the precipitates. The plate precipitate was divided by dislocation lines as shown by a green arrow in Fig. S4b. The $(2\overline{11}0)$ and $(\overline{11}20)$ planes of the trace line were marked by red lines in Fig. S4c, and there is an angle of ~29.8° between the trace line and the plane of the precipitate. It is observed that the mismatch is about 0.58 nm along the $[\overline{11}0]$ direction of the precipitate, which approximately corresponds to the distance between two neighboring atomic planes of the precipitate. This indicates that the precipitates with a size of 160 nm and mismatch of 0.58 nm along the $[\overline{11}0]$ direction are shearable.

3.3. *Texture evolution*

The EBSD IPF image and the pole figure of the alloys are illustrated in Fig. 5. The observation direction is along the ND-ED planes. With the addition of Mn, the number of blue and green grains increases, indicating that there are more $[10\bar{1}0]$- and $[2\overline{11}0]$-oriented grains. The c axis of $[10\bar{1}0]$- and $[2\overline{11}0]$-oriented grains are perpendicular to the ED. More grains in the $[10\bar{1}0]$ and $[2\overline{11}0]$ orientation indicate a stronger basal texture. Fig. 5 shows that the maximum pole figure intensity of the Mg-xMn-0.5Ce alloys increased from 8.83 to 30.42 with increasing Mn content.

3.4. *Mechanical properties of the as-extruded Mg-xMn-0.5Ce alloys*

The engineering stress-strain curves of the Mg-xMn-0.5Ce alloys are shown in Fig. S5. The test direction is along the 0°, 45°, and 90° angles of the sheets. Table 2 lists the corresponding values of TYS, ultimate tensile strength (UTS), and failure elongation (FE). With the addition of Mn, the TYS and the UTS are obviously improved. The FE increases first and then decreases. The Mg-0.9Mn-0.5Ce alloy shows the highest TYS and UTS in all directions compared to other alloys.

In general, the anisotropy of sheets at room temperature is significantly influenced by the r-value. According to Eq. (1) and Eq. (2), the r-values for Mg-xMn-0.5Ce alloys are obtained by conducting tensile tests, and the results are listed in Table 2. The Δr values for three sheets are 0.61, 0.49, and 0.34, respectively. The Mg-0.3Mn-0.5Ce alloy has the highest Δr, while the Mg-0.9Mn-0.5Ce alloy has the lowest Δr. For a given sheet, the r-value represents the plastic strain ratio. The larger the r-value, the more severe the anisotropy. Thus, the Mg-0.9Mn-0.5Ce alloy has the smallest value of Δr, indicating that the Mg-0.9Mn-0.5Ce alloy tends to be isotropic among the three sheets.

4. Discussion

4.1. *Microstructure variation as a function of Mn content*

In this study, the Mn content was increased from 0.3 wt% to 0.9 wt%, and the added Mn can be completely solid in the Mg matrix after heat treatment. The different content of Mn in the solid solution leads to different microstructures in the as-extruded Mg-0.5 wt%Ce alloy. Therefore, the effects of Mn on recrystallization behavior, microstructure evolution, and sandwich structure formation are studied in detail.

4.1.1. *DRXed behaviors with Mn content in solid solution*

It is known that the DRX process that occurs during extrusion is

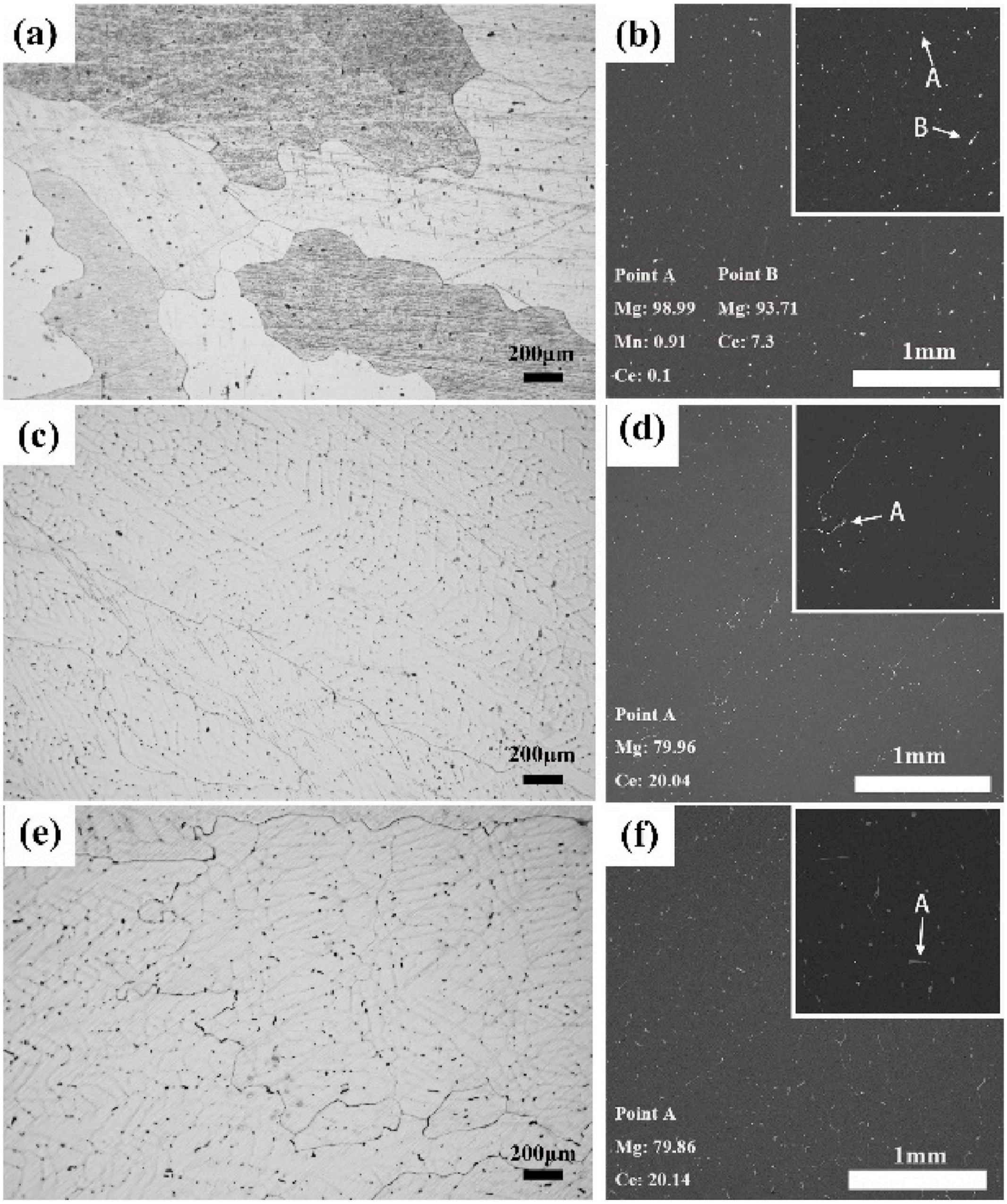

Fig. 2. (a) OM image and (b) BSE SEM image obtained from Mg-0.3Mn-0.5Ce alloy, (c) OM image and (d) BSE SEM image obtained from Mg-0.6Mn-0.5Ce alloy, (e) OM image and (f) BSE SEM image obtained from Mg-0.9Mn-0.5Ce alloy.

divided into two parts: nucleation and growth. In order to clarify the effect of Mn content in solid solution on DRX behavior, the influence of Mn in solid solution on nucleation and growth of DRXed grains is discussed.

Through the EBSD analysis method, the abovementioned mechanism of DRX can be identified in detail. As shown in Fig. 6, it is clear from the EBSD and TEM-HADDF map of the center part of the Mg-0.9Mn-0.5Ce sheet. From Fig. 6a, the large grains are surrounded by fine grains in the shape of a necklace. Fig. 6b confirms that these fine grains are DRXed grains. The (0001) orientation distribution of the fine DRXed grains is similar to that of the parent grains, as shown in Fig. 6a. In addition, the orientation of the DRXed grains is completely consistent with that of the deformed grains in the pole figure, as shown in Fig. S7. The main reason for the formation of this similar orientation is that these fine DRXed grains are influenced by the orientation of parent grains. In addition, the formed DRXed grains may be discontinuous dynamic recrystallization (DDRX), which proceeds by high-angle-grain boundaries (HAGBs) arching nucleation and grain boundary migration to make DRXed grains grow, and finally leads to the formation of the DRXed grains with the same texture as the parent grains.

In Fig. S6, the DRX distribution and relative frequency of as-extruded Mg-xMn-0.5Ce alloys exhibit that the volume of DRXed grains of three alloys are 80.38%, 51.78% and 27.83, respectively. And the volume of deformed grains of three alloys are 11.30%, 44.87% and 70.88%, respectively. It is showed that the volume of deformed grains is increase with Mn addition. And, these deformed grains often show a stronger basal texture. In addition, Grains formed by DDRX have a similar texture to the parent grains. In generally, the texture intensity of the Mg-0.9Mn-0.5Ce alloy stronger than that of the other two alloys. Furthermore, a small number of residual dislocations and second-phase particles are also found in Fig. 6d (as shown with a yellow arrow). These residual dislocations and particles can act as nucleation sites for DRX during

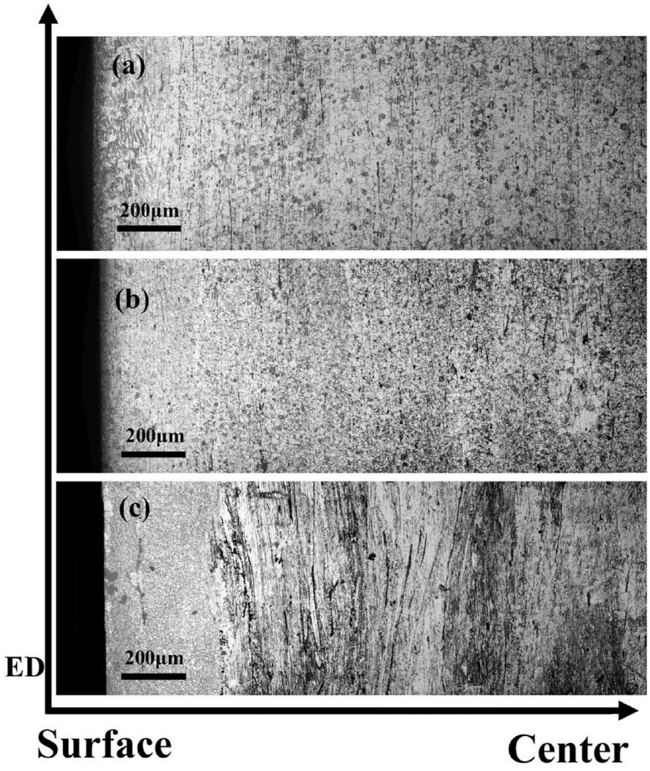

Fig. 3. Large-scale OM of the as-extruded alloy sheet, (a) the schematic of the observation position, (b) Mg-0.3Mn-0.5Ce alloy, (c) Mg-0.6Mn-0.5Ce alloy, and (d) Mg-0.9Mn-0.5Ce alloy.

extrusion. In Fig. 6b, there are DRXed grains around twins and second-phase particles. In the KAM map, a large number of nucleation points around twins and second-phase particles can also be found. Thus, a small number of residual dislocations and second-phase particles serve as nucleation sites for recrystallization in the extrusion process. In summary, there are a large number of LAGBs in the microstructure, which means that DDRX is the main DRX mechanism. In addition, twin dynamic recrystallization (TDRX) and particle stimulation nucleation (PSN) mechanisms also exist during extrusion.

When the DRXed grains nucleate, the second process will proceed: grain growth. The precipitates play a major role in suppressing the growth of DRXed grains. In the process of DRXed-grain growth, the second-phase particles will have a pinning effect on the grain boundary, thereby affecting the migration of the grain boundary [42]. The relationship between second-phase particles and grain growth can be summarized with the following equations [43]:

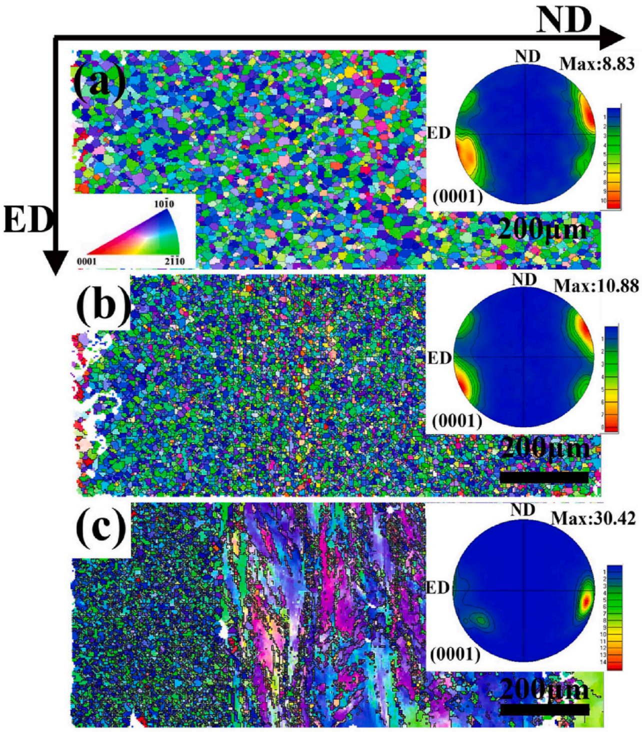

Fig. 5. EBSD IPF image and the corresponding pole figure of the as-extruded Mg-xMn-0.5Ce alloys, (a) Mg-0.3Mn-0.5Ce alloy, (b) Mg-0.6Mn-0.5Ce alloy, and (c) Mg-0.9Mn-0.5Ce alloy.

Table 2
The TYS, UTS, FE, *r*-value, and average *r*-value (Δ*r*) of the Mg-xMn-0.5Ce alloys (x = 0.3, 0.6, 0.9 wt%).

Sheets	Directions	TYS (MPa)	UTS (MPa)	FE (%)	*r*-value	Δ*r*
Mg-0.3Mn-0.5Ce	0°	86.5	186.9	13.4	0.53	0.61
	45°	113.3	200.9	11.4	0.65	
	90°	174.6	225.9	10.5	1.09	
Mg-0.6Mn-0.5Ce	0°	124.6	207.7	20.0	0.92	0.49
	45°	138.2	214.5	20.5	0.70	
	90°	159.5	225.7	14.5	1.19	
Mg-0.9Mn-0.5Ce	0°	166.7	233.1	17.7	0.41	0.34
	45°	167.6	227.6	18.4	0.57	
	90°	168.4	226.4	14.2	0.52	

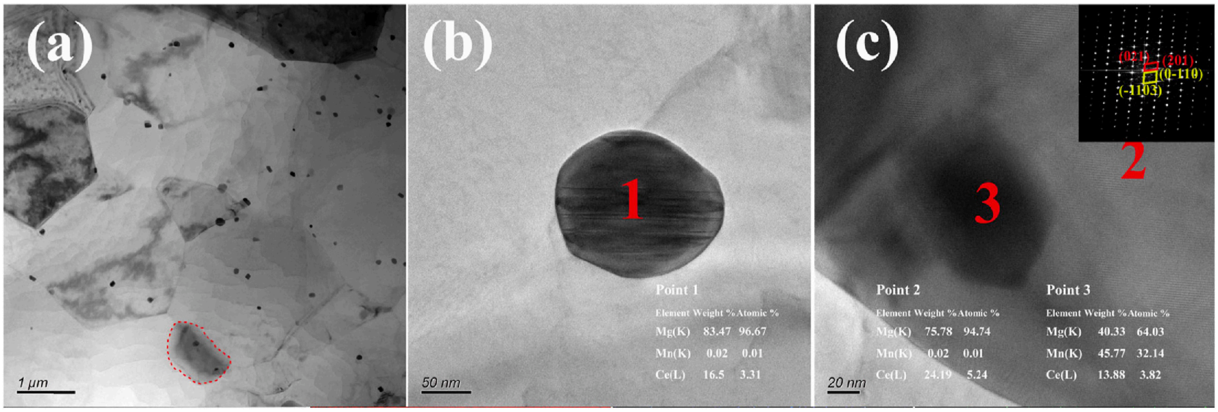

Point 1

Element	Weight %	Atomic %
Mg(K)	83.47	96.67
Mn(K)	0.02	0.01
Ce(L)	16.5	3.31

Point 2

Element	Weight %	Atomic %
Mg(K)	75.78	94.74
Mn(K)	0.02	0.01
Ce(L)	24.19	5.24

Point 3

Element	Weight %	Atomic %
Mg(K)	40.33	64.03
Mn(K)	45.77	32.14
Ce(L)	13.88	3.82

Fig. 4. (a)The BF-TEM images of the as-extruded Mg-0.9Mn-0.5Ce alloy, (b) and (c) local higher magnification of (a).

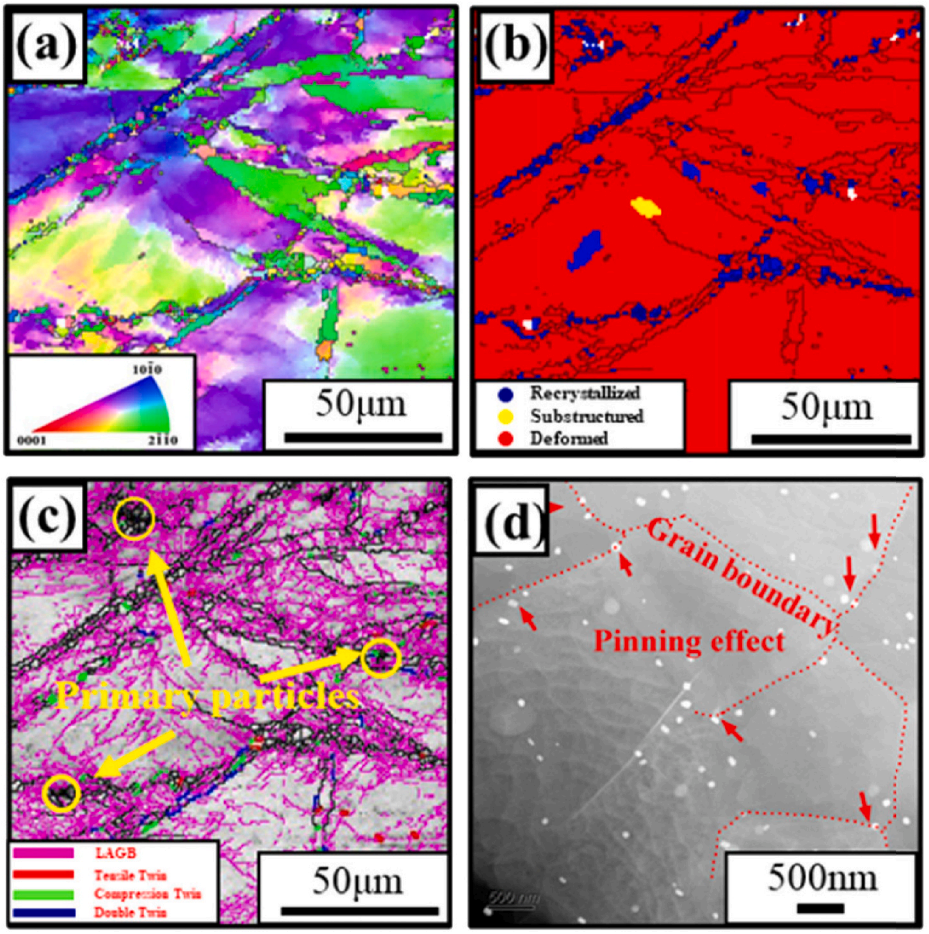

Fig. 6. The EBSD and HADDF map results for the center part of the Mg-0.9Mn-0.5Ce sheet: (a) IPF map; (b) DRX distribution map; (c) PSN map; and (d) HADDF map images.

$$V = M_0 \exp\left(-\frac{Q}{RT}\right)\left(P_D^{\mathrm{Rex}} - P_Z - P_C\right) \tag{3}$$

$$P_Z = \frac{3F_v\gamma}{2r} \tag{4}$$

where M_0 is the constant of boundary migration, Q is the activation energy, R is the gas constant, T is the deformation temperature, P_D^{Rex} is the recrystallization driving force, P_Z is the Zener pinning stress, P_C is the boundary curvature stress, F_v is the volume of the second phase, γ is the energy of the grain boundary, and r is the average radius of second phase. Thus, the grain boundary migration rate mainly depends on the difference between the recrystallization driving force and the pinning stress. The pinning stress hinges on the volume fraction and size of precipitates. The smaller the size and the larger the number of precipitates, the stronger the pinning effect. In the HADDF map (Fig. 6d), it can be observed that the precipitated phase is distributed inside the grains and along the grain boundaries. These precipitated phases, which are distributed along the grain boundary, will hinder the migration of the grain boundary, thereby forming fine DRXed grains. In this work, when the Mn content increases to 0.9 wt%, the volume of precipitated α-Mn phase will increase, and the pinning effect of α-Mn will be enhanced, thus the fine DRXed grains are formed. At the same time, precipitated phases also hinder the migration of the parent grain boundary, and coarse un-DRXed grains are formed. Hence, both coarse un-DRXed grains and fine DRXed grains structures are formed.

4.1.2. The origin of sandwich microstructure

When the Mn increases to 0.9 wt%, a sandwich structure is formed. The sandwich structure contains a surface layer with uniform equiaxed grains and a center part with elongated un-DRXed grains and fine DRXed grains. During the extrusion process, the distribution of stress from the surface of the material to the center is different, and the structure formed is also different. To understand the formation mechanism of this sandwich structure, the distribution of internal residual stress in the extruded alloy was studied. The KAM map of the Mg-0.9Mn-0.5Ce sheet and the formation of the sandwich structure are illustrated in Fig. 7. From Fig. 7a, it is found that the KAM value for the Mg-0.9Mn-0.5Ce sheet presents a gradient distribution, which increases gradually from the surface to the center, and significant unfinished microstructure (unDRXed microstructure) is retained. What's more, the large strain on the surface of the sample is easier to nucleate, while the low strain in the center part is not easy to nucleate, so considerable strain remains inside.

Based on previous analysis of the DRX process and strain distribution, the nucleation and growth process can be summarized as follows (Fig. 7b):

1. First, the sample is undergoing a long period of solution treatment before extrusion, and the solid-solution atoms are dissolving in the matrix to form a single-phase, solid-solution alloy.
2. In the initial stage of extrusion, the strain of the sample has a gradient distribution in the thickness direction. Due to the different forces of the extrusion cylinder, the surface strain of the sample is the largest, while the central strain of the sample is small. Therefore, more dislocations, sub-grain boundaries, and precipitates are generated on the surface rather than in the center of the sample, which provides many nucleation points for the subsequent extrusion

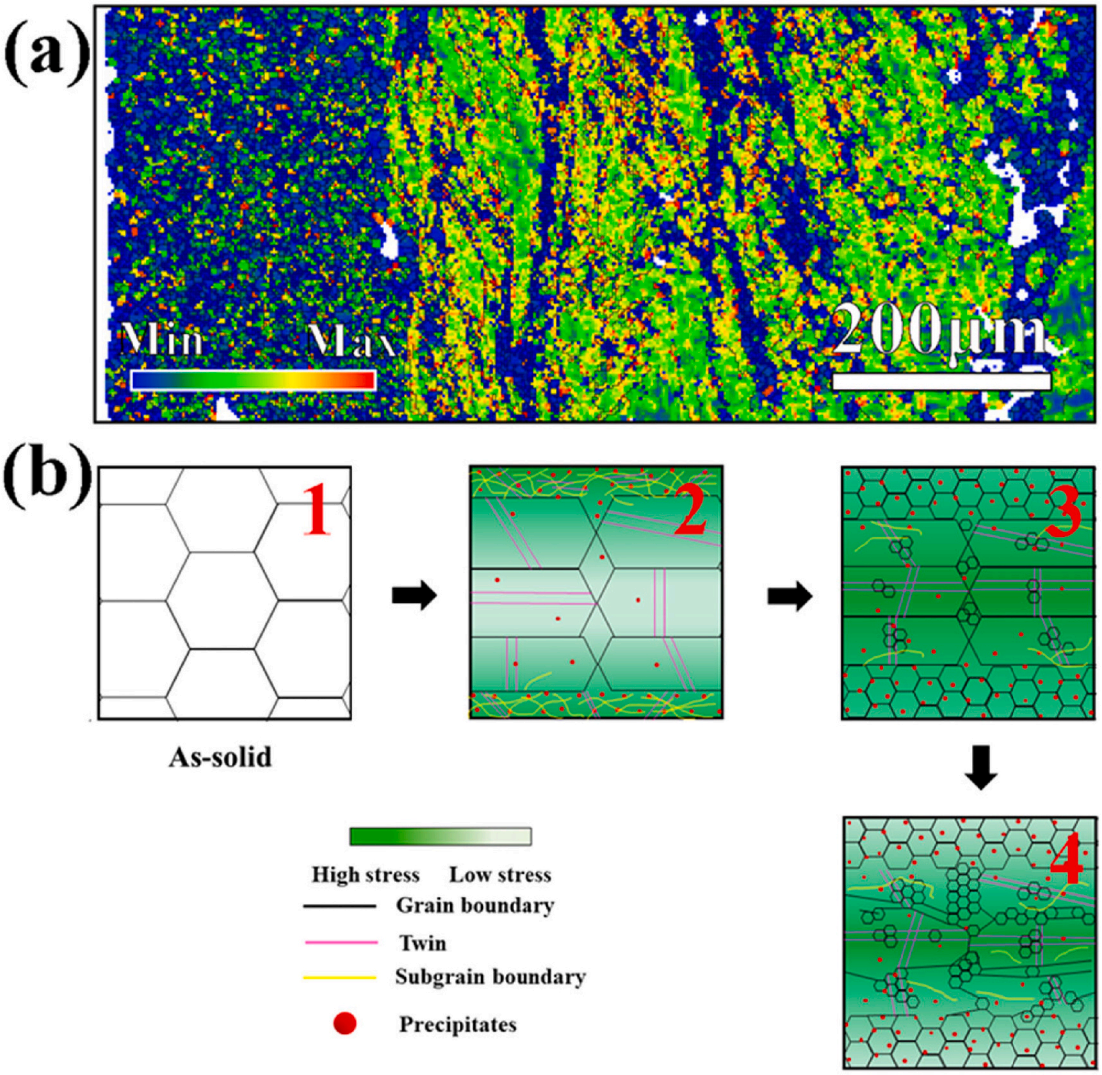

Fig. 7. (a) KAM maps of as-extruded Mg-0.9Mn-0.5Ce alloys; (b) Schematic diagram of sandwich structure formation during extrusion.

process. At the same time, the high strain at the surface provides a higher driving force for DRX, while the low strain at the center provides a lower driving force for DRX.

3. In this situation, due to more defects and larger strain on the surface, the surface nucleation ratio is higher than the center nucleation ratio. The surface layer forms a DRX grain structure and the center layer still maintains a deformed grain structure.
4. Finally, due to the formation of more precipitated phases and the pinning effect on the surface than in the center. Thus, fine DRXed grains are formed on the surface and consume the storage energy and dislocations at the surface. At the same time, the grain boundary at the center is also pinned by the precipitated phases, and a bimodal grain structure forms.

4.2. *Evolution of mechanical properties*

In this work, the improved mechanical strength of as-extruded Mg–xMn-0.5Ce alloys are due mostly to the second-phase strengthening, grain-refining strengthening, texture strengthening and solid-solution strengthening. However, due to the limited solubility of Mn content in the alloy at room temperature, the solution strengthening effect is not discussed here.

4.2.1. *Strengthening mechanism of second-phase particles*

The second-phase particles are an important and complex consideration for the improvement of mechanical properties, which are influenced by their size, morphology, and distribution. In the Orowan relationship, the TYS is based on the particle size (*d*) and volume fraction (*f*) of the second phase [44]:

$$\mathrm{YS}\propto f^{\frac{1}{2}}d^{-1}Ind \tag{5}$$

Obviously, the YS could be improved by reducing the particle size and increasing the volume fraction. In this work, the Ce content is the same, while the Mn content is different. With the increase in Mn content, the volume of α-Mn precipitate will increase. Therefore, the effect of Orowan strengthening is increased by increasing the Mn content. Our previous work [4,29,45] showed that when the Mn content increases to 1 wt%, the TYS increases by 20–30 MPa. In this work, when the Mn content increases to 0.9 wt%, the TYS of the ED direction increases by 80 MPa (190%). Furthermore, referring to the research work of Mg alloys, which contains Mn [8,28,29,46], the TYS improvement with Mn particles cannot reach 190% or 80 MPa, which is far below this value. Hence, the enhanced TYS of the Mg–Mn-0.5Ce alloy is not only related to the Mn particles, but also to other strengthening factors.

4.2.2. *Strengthening mechanism of grain size*

Grain size is a crucial parameter that affects the mechanical properties of alloys. The engineering stress-strain curves are shown in Fig. S5. With the incremental increase in Mn content, the YS increases with the decreasing average grain size. The Hall-Petch (H–P) relationship can be used to analyze the strengthening mechanism of grain size on YS, as follows [47]:

$$\sigma_{GB} = kd^{-1/2} \tag{6}$$

where k is the coefficient of HP related to alloys, and d is the average grain size of alloys. The YS is inversely proportional to the grain size. This implies that the finer grains bring more grain-boundary strengthening, and thus present a better strengthening effect. The Mg-0.3Mn-0.5Ce and Mg-0.6Mn-0.5Ce alloys exhibit a relatively uniform grain structure, while the Mg-0.9Mn-0.5Ce alloy has a bimodal microstructure containing DRXed and un-DRXed grains. The grain-boundary strengthening of the Mg-0.3Mn-0.5Ce and Mg-0.6Mn-0.5Ce alloys can be evaluated by the HP relationship directly. However, the grain-boundary strengthening of the Mg-0.9Mn-0.5Ce alloy should be divided into two parts [28]:

$$\sigma_{gs} = \sigma_{Re} V_{Re} + \sigma_{Un} V_{Un} \tag{7}$$

where σ_{gs} is the grain-boundary strength of bimodal grains, σ_{Re} and σ_{Un} are the YS of DRXed grains and un-DRXed grains and V_{Re} and V_{Un} are the volume fraction of DRXed grains and un-DRXed grains, respectively. According to the EBSD result (Fig. 5), the volume fractions of DRXed grain and un-DRXed grain structure of the Mg-0.9Mn-0.5Ce alloy are 25% and 75%, respectively. The average grain size of the DRXed grains and un-DRXed grains are 3.57 μm and 12.88 μm, respectively. Moreover, the average grain size of the Mg-0.3Mn-0.5Ce and Mg-0.6Mn-0.5Ce alloys are 12.08 μm and 6.38 μm, respectively. Therefore, the grain boundary strengthening can be calculated be calculated by Eq. (6) and Eq. (7), and thus the strengthening value of Mg-0.9Mn-0.5Ce alloy is 121% for Mg-0.3Mn-0.5Ce alloy, and 87% for Mg-0.6Mn-0.5Ce alloy.

4.2.3. Strengthening mechanism of the texture

To analyze the influence of texture on the TYS, the YS versus the Schmid factor (SF) for basal<a> slip is shown in Fig. 8. The relationship between the YS and the SF for basal<a> slip can be shown by Ref. [48]:

$$\sigma_s = \tau / m_s \tag{8}$$

where τ is the CRSS of basal<a> slip and m_s is the SF of basal<a> slip.

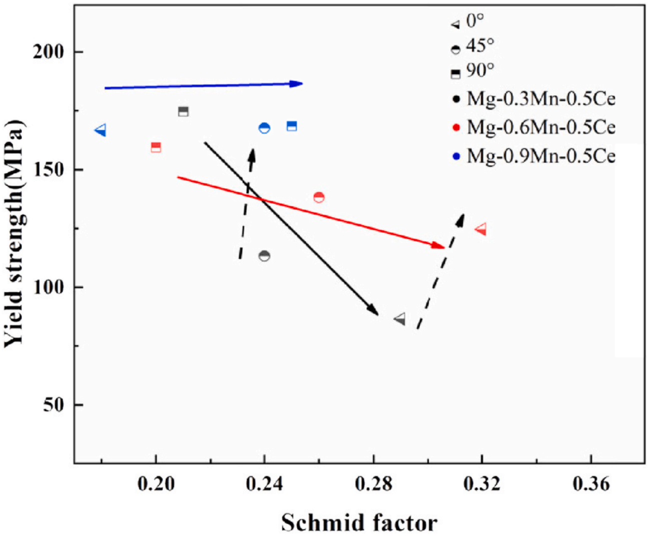

Fig. 8. The yield strength as a function of average Schmid factor for basal<a> slip in the Mg-0.3Mn-0.5Ce, Mg-0.6Mn-0.5Ce, and Mg-0.9Mn-0.5Ce alloy sheets along the three tensile directions at room temperature.

The yield strength is inversely proportional to the SF of basal<a> slip. Therefore, the TYS tends to improve when the SF has a lower value. The low SF value means that the grain orientations are not favorable to basal slip, which enhance yield strength [49]. It can be found that the Mg-0.9Mn-0.5Ce alloy has the lowest SF in the three directions compared with the other two alloys. The lowest SF value is attributed to the sandwich grain structure of the Mg-0.9Mn-0.5Ce alloy, which consists of small DRXed grains and coarse un-DRXed grains. The orientation of these un-DRXed grains is parallel to the tensile axis, causing a low SF for basal<a> slip. In addition, most of the fine DRXed grains are in the direction of $[10\bar{1}0]$ and $[2\bar{1}\bar{1}0]$, which is also parallel to the loading direction. Therefore, high stress is needed to activate basal<a> slip, which improves the TYS of the Mg-0.9Mn-0.5Ce alloy.

4.3. Effect of sandwich-like grained microstructure on the anisotropy

Wrought Mg alloy sheets usually have a strong basal texture, which induces mechanical anisotropy. The mechanical anisotropy makes it difficult for Mg sheets to deform further. It is important to overcome this difficulty with wrought Mg alloys. Like gradient structured (GS) materials, sandwich-like grain structure materials can improve the deformation mechanism and mechanical properties and have a significant impact on anisotropy. This can be analyzed and discussed from two points-of-view: grain structure distribution and grain orientation.

On the one hand, from the point-of-view of grain structure distribution, the sandwich-like grain structure is similar to GS materials. According to reports, the deformation mechanism of GS materials has been studied through computer simulations. Zeng et al. [50] used the crystal plasticity finite element model and found that there is a large stress/strain gradient in GS Cu under uniaxial load. In order to adapt to the incompatibility of deformation, a gradient variation of GS Cu was established, which leads to an increase in certain mechanical properties. On the other hand, in order to coordinate the non-uniform deformation of GS materials (specifically, IF steel and GS Cu [51–53]), a large number of geometrically necessary dislocations (GNDs) must be stored in the microstructure. The GNDs are the origin of the back stress. They have a significant strengthening effect on GS IF steel and GS Cu, which improves the mechanical properties of the sample. In this paper, it is found that the anisotropy of the Mg-0.9Mn-0.5Ce alloy with a sandwich-like structure is significantly smaller than that of the other two alloys in Fig. S5. The main reason is that the deformation mechanism of the sandwich-like grain structure is similar to the GS material. Hence, the stress state between the surface and the core is different; that is, a stress gap exists in the thickness of the sheet. During the initial process of deformation, the sandwich-like grain structure sample undergoes elastic-plastic deformation. The coarse-grained layer first begins to plastically deform, while the fine-grained layer on the surface remains elastically deformed. Hence, an elastic-plastic deformation interface is formed between the fine-grained layer and the coarse-grained layer. When the strain increases, this interface will coordinate the non-uniform plastic deformation between the fine-grained and the coarse-grained so that they deform together. Hence, the deformation of the sample in all directions tends to be uniform. In addition, due to the existence of a stress gap, there may be a large number of GNDs between the surface and the core, resulting in back stress. Back stress provides additional strain at the initial stage of elastic-plastic deformation. Finally, the TYS of the Mg-0.9Mn-0.5Ce alloy is improved.

Grain orientation is also an important factor affecting the mechanical anisotropy of the Mg alloy. In this work, the SF values of the Mg-0.9Mn-0.5Ce alloy are lower than the other two alloys. Meanwhile, the difference in SF values at 0°, 45° and 90° is also less than that of the other two samples. This indicates that for the lower SF values of the Mg-0.9Mn-0.5Ce alloy, it is hard to initiate the basal<a> slip, and this results in a higher TYS. The small difference of SF values in various directions has a similar effect on the activation of the basal<a> slip, showing almost equal TYS values. On the contrary, for the higher SF value, it is easy to activate the basal<a> slip, and this induces a lower TYS. The sharp difference among SF values in various directions causes a completely different degree of difficulty in activating basal<a> slip, which indicates a strong yield anisotropy. From Fig. 8, the Mg-0.9Mn-0.5Ce alloy with the smallest difference among SF values in various directions results in a weak yield anisotropy.

5. Conclusions

In this work, the effect of solid-solution Mn content on the evolution of the microstructure and on mechanical properties of the Mg-0.5 wt% Ce alloys has been studied. The main conclusions are as follows:

1. With the Mn addition, the grain size of as-extruded Mg–Mn–Ce alloy was significantly refined from 12.67 μm to 3.96 μm. The Mg-0.9Mn-0.5Ce alloy exhibited a sandwich-like grain structure, which consisted of fine grains on the surface and bimodal grains in the center.
2. The Mg-0.9Mn-0.5Ce alloy sheet presented better comprehensive mechanical properties than other alloys. The Mg-0.9Mn-0.5Ce alloy sheet exhibited and isotropic yield, and TYS along 0°, 45°, and 90° were 166.7, 167.6, and 168.4 MPa, respectively.
3. Sandwich-like grain structure is formed due to the combination of the gradient strain in the extrusion cylinder and the pinning effect of the nanoscale α-Mn particles. The large strain on the surface induced the formation of fine grains, and the pinning effect of nanoscale α-Mn particles assisted in grain refinement. The α-Mn particles, which were also located at the unDRXed grain boundaries, delayed the DRX process.
4. The improved mechanical properties resulted in second-phase strengthening, grain-boundary strengthening, and grain orientation. The grain-boundary strengthening was the dominant strengthening mechanism. The modified anisotropy was attributed to the small difference among the SF values in the three directions. The Mg-0.9Mn-0.5Ce alloy sheet with the sandwich structure has the advantages of low alloy content, good mechanical properties, and a simple manufacturing process, all of which indicate good development prospects and the need for in-depth research in the future.

CRediT authorship contribution statement

Shibo Zhou: Conceptualization, Methodology, Software, Formal analysis, Investigation, writing—original draft preparation. **Peng Peng:** Methodology, Validation, Formal analysis, Investigation, Data curation, writing—review and editing. **Tingting Liu:** Conceptualization, Methodology, Validation, Formal analysis, Investigation, Resources, Data curation, writing—review and editing, Supervision, Funding acquisition. **Guangmin Sheng:** Validation, Supervision. **Jia She:** Supervision, Funding acquisition, All authors have read and agreed to the published version of the manuscript. **Fusheng Pan:** Validation, Investigation, Resources, Supervision, Funding acquisition, P.F, Data curation.

Declaration of competing interest

The authors declare that they have no known competing financial interests or personal relationships that could have appeared to influence the work reported in this paper.

Acknowledgements

This research was funded by National Natural Science Foundation of China (51531002, 51971042, 51901028), the National Key Research and Development Program of China (2016YFB0301100), Youth Project of Science and Technology Research Program of Chongqing Education Commission of China (KJ201903136636560), and the Chongqing Academician Special Fund (cstc2018jcyj-yszxX0007, cstc2019yszx-jcyjX0004, cstc2020yszx-jcyjX0001, cstc2018jcyjAX0070). The authors would like to thank joint lab for electron microscopy of Chongqing University. This work was supported by Sinoma Institute of Materials Research (Guang Zhou) Co., Ltd (SIMR). We thank TopEdit (www.topeditsci.com) for its linguistic assistance during the preparation of this manuscript.

Appendix A. Supplementary data

Supplementary data to this article can be found online at https://doi.org/10.1016/j.msea.2021.141567.

References

[1] E. Karakulak, A review: past, present and future of grain refining of magnesium castings, J. Magnes. Alloy 7 (3) (2019) 355–369.

[2] J. Song, J. She, D. Chen, F. Pan, Latest research advances on magnesium and magnesium alloys worldwide, J. Magnes. Alloy 8 (1) (2020) 1–41.

[3] T. Xu, Y. Yang, X. Peng, J. Song, F. Pan, Overview of advancement and development trend on magnesium alloy, J. Magnes. Alloy 7 (3) (2019) 536–544.

[4] J. She, P. Peng, L. Xiao, A.T. Tang, Y. Wang, F. Pan, Development of high strength and ductility in Mg–2Zn extruded alloy by high content Mn-alloying, Mater. Sci. Eng., A 765 (2019).

[5] C. Liu, X. Chen, W. Zhang, Y. Zhang, F. Pan, Microstructure, creep behavior and corrosion resistance in the ultrafine-grained surface layer of Mg-6Zn-0.2Y-0.4Ce-0.5Zr alloy processed by surfacing friction treatment, Mater. Sci. Eng., A 776 (2020).

[6] Y.Z. Du, X.G. Qiao, M.Y. Zheng, K. Wu, S.W. Xu, Development of high-strength, low-cost wrought Mg–2.5mass% Zn alloy through micro-alloying with Ca and La, Mater. Des. 85 (2015) 549–557.

[7] H. Pan, G. Qin, Y. Huang, Y. Ren, X. Sha, X. Han, Z.Q. Liu, C. Li, X. Wu, H. Chen, C. He, L. Chai, Y. Wang, J.f. Nie, Development of low-alloyed and rare-earth-free magnesium alloys having ultra-high strength, Acta Mater. 149 (2018) 350–363.

[8] H. Liao, J. Kim, T. Liu, A. Tang, J. She, P. Peng, F. Pan, Effects of Mn addition on the microstructures, mechanical properties and work-hardening of Mg-1Sn alloy, Mater. Sci. Eng., A 754 (2019) 778–785.

[9] Q. Wang, Y. Shen, B. Jiang, A. Tang, J. Song, Z. Jiang, T. Yang, G. Huang, F. Pan, A micro-alloyed Mg-Sn-Y alloy with high ductility at room temperature, Mater. Sci. Eng., A 735 (2018) 131–144.

[10] G. Zhu, L. Wang, H. Zhou, J. Wang, Y. Shen, P. Tu, H. Zhu, W. Liu, P. Jin, X. Zeng, Improving ductility of a Mg alloy via non-basal <a> slip induced by Ca addition, Int. J. Plast. 120 (2019) 164–179.

[11] Z.H. Li, T.T. Sasaki, M.Z. Bian, T. Nakata, Y. Yoshida, N. Kawabe, S. Kamado, K. Hono, Role of Zn on the room temperature formability and strength in Mg–Al–Ca–Mn sheet alloys, J. Alloys Compd. 847 (2020).

[12] B.Q. Shi, R.S. Chen, W. Ke, Solid solution strengthening in polycrystals of Mg–Sn binary alloys, J. Alloys Compd. 509 (7) (2011) 3357–3362.

[13] H. Somekawa, D. Egusa, E. Abe, Grain boundary plasticity in solid solution Mg–Li binary alloy, Mater. Sci. Eng., A 790 (2020).

[14] L. Gao, R.S. Chen, E.H. Han, Solid solution strengthening behaviors in binary Mg–Y single phase alloys, J. Alloys Compd. 472 (1–2) (2009) 234–240.

[15] S. Sandlöbes, M. Friák, S. Zaefferer, A. Dick, S. Yi, D. Letzig, Z. Pei, L.F. Zhu, J. Neugebauer, D. Raabe, The relation between ductility and stacking fault energies in Mg and Mg–Y alloys, Acta Mater. 60 (6–7) (2012) 3011–3021.

[16] N. Stanford, R.K.W. Marceau, M.R. Barnett, The effect of high yttrium solute concentration on the twinning behaviour of magnesium alloys, Acta Mater. 82 (2015) 447–456.

[17] Z. Wu, R. Ahmad, B. Yin, S. Sandloebes, W.A. Curtin, Mechanistic origin and prediction of enhanced ductility in magnesium alloys, Sci 359 (6374) (2018) 447–451.

[18] Z.H. Huang, L.Y. Wang, B.J. Zhou, T. Fischer, S.B. Yi, X.Q. Zeng, Observation of non-basal slip in Mg-Y by in situ three-dimensional X-ray diffraction, Scripta Mater. 143 (2018) 44–48.

[19] J.H. Zhang, S.J. Liu, R.Z. Wu, L.G. Hou, M.L. Zhang, Recent developments in high-strength Mg-RE-based alloys: focusing on Mg-Gd and Mg-Y systems, J. Magnes. Alloy 6 (3) (2018) 277–291.

[20] N.B. Tork, H. Saghafian, S.H. Razavi, K.J. Al-Fadhalah, R. Ebrahimi, R. Mahmudi, Microstructure and texture characterization of Mg-Al and Mg-Gd binary alloys processed by simple shear extrusion, Journal of Materials Research and Technology-Jmr&T 8 (1) (2019) 1288–1299.

[21] B.L. Wu, G. Wan, X.H. Du, Y.D. Zhang, F. Wagner, C. Esling, The quasi-static mechanical properties of extruded binary Mg-Er alloys, Mater. Sci. Eng., A 573 (2013) 205–214.

[22] Y. Chino, M. Kado, M. Mabuchi, Compressive deformation behavior at room temperature-773 K 14 in Mg-0.2 mass%(0.035at.%)Ce alloy, Acta Mater. 56 (3) (2008) 387–394.

[23] Y. Chino, M. Kado, M. Mabuchi, Enhancement of tensile ductility and stretch formability of magnesium by addition of 0.2 wt%(0.035 at%)Ce, Mater. Sci. Eng., A 494 (1–2) (2008) 343–349.

[24] T. Liu, F. Pan, Development and application of "solid solution strengthening and ductilizing" for magnesium alloys, Chin. J. Nonferrous Metals 29 (9) (2019) 2050–2063.

[25] Z.W. Yu, A.T. Tang, C.Y. Li, J.G. Liu, F.S. Pan, Effect of manganese on the microstructure and mechanical properties of magnesium alloys, Int. J. Mater. Res. 110 (11) (2019) 1016–1024.

[26] P. Peng, X. He, J. She, A. Tang, M. Rashad, S. Zhou, G. Zhang, X. Mi, F. Pan, Novel low-cost magnesium alloys with high yield strength and plasticity, Mater. Sci. Eng., A 766 (2019).

[27] F. Hu, S. Zhao, G. Gu, Z. Ma, G. Wei, Y. Yang, X. Peng, W. Xie, Strong and ductile Mg-0.4Al alloy with minor Mn addition achieved by conventional extrusion, Mater. Sci. Eng., A 795 (2020).

[28] T.S. Zhao, Y.B. Hu, B. He, C. Zhang, T.X. Zheng, F.S. Pan, Effect of manganese on microstructure and properties of Mg-2Gd magnesium alloy, Mater. Sci. Eng., A 765 (2019) 10.

[29] S. Zhou, X. He, P. Peng, T. Liu, G. Sheng, A. Tang, F. Pan, Achieving high yield strength and ductility in as-extruded Mg-0.5Sr alloy by high Mn-alloying, Materials 13 (18) (2020).

[30] T. Chen, X. Xiong, Y. Yuan, A. Tang, D. Li, A. Atrens, F. Pan, Effect of steels on the purity of molten Mg alloys, Adv. Eng. Mater. 22 (11) (2020).

[31] Liu Yao, Zeng, Lei Li, Du Li, Effect of manganese on microstructure and corrosion behavior of the Mg-3Al alloys, Metals 9 (4) (2019).

[32] D. Gu, J. Peng, J. Wang, Z. Liu, F. Pan, Effect of Mn modification on the corrosion susceptibility of Mg–Mn alloys by magnesium scrap, Acta Metall. Sin. 34 (2020) 1–11.

[33] Z.W. Yu, A.T. Tang, Q. Wang, Z.Y. Gao, J.J. He, J. She, K. Song, F. Pan, High strength and superior ductility of an ultra-fine grained magnesium-manganese alloy, Materials Science and Engineering a-Structural Materials Properties Microstructure and Processing 648 (2015) 202–207.

[34] G. Liu, J. Zhang, Y. Dou, First-principles study of solute–solute binding in magnesium alloys, Computational Materials ence 103 (2015) 97–104.

[35] J. Zhang, Y. Dou, G. Liu, Z. Guo, First-principles study of stacking fault energies in Mg-based binary alloys, Computational Materials ence 79 (2013) 564–569.

[36] C. Fang, J. Zhang, F. Pan, First-principles study on solute-basal dislocation interaction in Mg alloys, J. Alloys Compd. 785 (2019) 911–917.

[37] Q. Wang, B. Jiang, Y. Chai, B. Liu, S. Ma, J. Xu, F. Pan, Tailoring the textures and mechanical properties of AZ31 alloy sheets using asymmetric composite extrusion, Mater. Sci. Eng., A 673 (2016) 606–615.

[38] J. Jiang, S. Ni, H. Yan, N. Yan, M. Song, $\langle c + a \rangle$ dislocations shearing (0001)α plate precipitates in an Mg-Zn-Mn alloy, Scripta Mater. 170 (2019) 24–28.

[39] J. Wang, N. Stanford, Investigation of precipitate hardening of slip and twinning in Mg5%Zn by micropillar compression, Acta Mater. 100 (2015) 53–63.

[40] J.J. Bhattacharyya, F. Wang, N. Stanford, S.R. Agnew, Slip mode dependency of dislocation shearing and looping of precipitates in Mg alloy WE43, Acta Mater. 146 (2018) 55–62.

[41] Z. Huang, C. Yang, L. Qi, J.E. Allison, A. Misra, Dislocation pile-ups at β1 precipitate interfaces in Mg-rare earth (RE) alloys, Mater. Sci. Eng., A 742 (2019) 278–286.

[42] J.D. Robson, D.T. Henry, B. Davis, Particle effects on recrystallization in magnesium–manganese alloys: particle pinning, Mater. Sci. Eng., A 528 (12) (2011) 4239–4247.

[43] H.Y. Wang, J. Rong, G.J. Liu, M. Zha, C. Wang, D. Luo, Q.C. Jiang, Effects of Zn on the microstructure and tensile properties of as-extruded Mg-8Al-2Sn alloy, Mater. Sci. Eng., A 698 (2017) 249–255.

[44] J.F. Nie, Effects of precipitate shape and orientation on dispersion strengthening in magnesium alloys, Scripta Mater. 48 (8) (2003) 1009–1015.

[45] J. She, S.B. Zhou, P. Peng, A.T. Tang, Y. Wang, H.C. Pan, C.L. Yang, F. Pan, Improvement of strength-ductility balance by Mn addition in Mg–Ca extruded alloy, Mater. Sci. Eng., A 772 (2020).

[46] J. She, F.S. Pan, W. Guo, A.T. Tang, Z.Y. Gao, S.Q. Luo, K. Song, Z.W. Yu, M. Rashad, Effect of high Mn content on development of ultra-fine grain extruded magnesium alloy, Mater. Des. 90 (2016) 7–12.

[47] P. Peng, J. She, A. Tang, J. Zhang, S. Zhou, X. Xiong, F. Pan, Novel continuous forging extrusion in a one-step extrusion process for bulk ultrafine magnesium alloy, Mater. Sci. Eng., A 764 (2019).

[48] J.A. del Valle, F. Carreño, O.A. Ruano, Influence of texture and grain size on work hardening and ductility in magnesium-based alloys processed by ECAP and rolling, Acta Mater. 54 (16) (2006) 4247–4259.

[49] T. Chen, Z. Chen, L. Yi, J. Xiong, C. Liu, Effects of texture on anisotropy of mechanical properties in annealed Mg–0.6%Zr–1.0%Cd sheets by unidirectional and cross rolling, Mater. Sci. Eng., A 615 (2014) 324–330.

[50] Z. Zeng, X. Li, D. Xu, L. Lu, H. Gao, T. Zhu, Gradient plasticity in gradient nano-grained metals, Extreme Mechanics Letters 8 (2016) 213–219.

[51] X. Yang, X. Ma, J. Moering, H. Zhou, W. Wang, Y. Gong, J. Tao, Y. Zhu, X. Zhu, Influence of gradient structure volume fraction on the mechanical properties of pure copper, Mater. Sci. Eng., A 645 (2015) 280–285.

[52] Y. Lin, J. Pan, H.F. Zhou, H.J. Gao, Y. Li, Mechanical properties and optimal grain size distribution profile of gradient grained nickel, Acta Mater. 153 (2018) 279–289.

[53] X. Li, L. Lu, J. Li, X. Zhang, H. Gao, Mechanical properties and deformation mechanisms of gradient nanostructured metals and alloys, Nature Reviews Materials 5 (9) (2020) 706–723.